Geophysical Research Letters®

Key Points:

- We introduce a particle-based model in investigating Aeolian (wind-blown) sand transport when the sand cover on the soil is sparse
- The scaling of the Aeolian transport rate with the wind shear velocity has a dependency on the sand cover thickness
- There is an anomaly in the functional dependence of the transport rate on the sand cover thickness, depending on the rigid ground roughness

Scaling Laws in Aeolian Sand Transport Under Low Sand Availability

Sandesh Kamath[1,2] [ID]**, Yaping Shao[1], and Eric J. R. Parteli[2]** [ID]

[1]Institute of Geophysics and Meteorology, University of Cologne, Cologne, Germany, [2]Faculty of Physics, University of Duisburg-Essen, Duisburg, Germany

Abstract Previous studies of wind-blown sand have considered either fully erodible or non-erodible soils, but the transport over sparsely sand-covered soils is still poorly understood. The quantitative modeling of this transport is important for parameterizing Aeolian processes under low sand availability. Here we show, by means of numerical simulations, that the sand transport rate Q scales with the wind shear velocity u_* as $Q = a \cdot \left[1 + b \cdot (u_*/u_{*t} - 1) \right] \cdot \sqrt{d/g} \cdot \rho_f \cdot \left(u_*^2 - u_{*t}^2 \right)$, where u_{*t} is the minimal threshold u_* for sustained transport, d is particle size, g is gravity and ρ_f is air density, while u_{*t} and the empirical parameters a and b depend on the sand cover thickness. Our model explains the transition from the quadratic to cubic scaling of Q with u_* as soil conditions change from fully erodible to rigid and provides constraints for modeling Aeolian transport under low sand availability.

Plain Language Summary The transport of sand by wind shapes the Earth's surface and constitutes one major factor for the emission of dust aerosols. The accurate modeling of wind-blown sand transport is thus important to achieve reliable climate simulations and to make predictions about the propagation of desertification. Previous models of wind-blown sand were designed to compute sand transport rates over a thick sand layer, such as the surface of large, active sand dunes. However, natural soils encompass a broad range of low sand availability conditions, such as crusted or bare soils. It has been a long-standing open question how wind-blown sand transport rates respond to wind velocity when the bare ground is covered by a thin layer of sand. Here we calculate the trajectories of wind-blown sand grains and find that sand transport rates increase faster with wind speed under low sand availability conditions than over sand dunes. The reason for this behavior is elucidated in our simulations: The hopping sand grains fly higher the less sand is covering the hard surface. We obtain mathematical expressions for the sand transport rates as a function of the thickness of sand covering the bare soil, which will be important to improve climate models.

1. Introduction

Aeolian (wind-blown) sand transport produces ripples and dunes and plays a vital role in shaping the Earth's surface. This transport occurs mainly through sand grains hopping along the surface (saltation), thereby transferring to the ground momentum that may set new particles into hopping, rolling or sliding motion (Bagnold, 1941; Kok et al., 2012; Shao, 2008). Furthermore, the particle splash generated by saltating grains provides one main mechanism of dust aerosol emission (Gillette, 1981; Shao et al., 1993), which has major feedbacks with the biosphere, the hydrological cycle and various other components of the Earth system (Mahowald et al., 2014; Schepanski, 2018). The accurate modeling of wind-blown sand is, thus, important for the development of reliable geomorphodynamic, climate and Earth system models (Shao, 2008).

Indeed, previous models of Aeolian transport focused mainly on the transport over either fully erodible beds, such as migrating dunes and ripples (Almeida et al., 2008; Anderson & Haff, 1988; Comola et al., 2019; Kok & Renno, 2009; Lämmel et al., 2012; Pähtz et al., 2014; Sauermann et al., 2001; Shao & Li, 1999), or rigid, fully non-erodible beds, such as consolidated dunes and bare soils (Ho et al., 2011). These studies have shown that wind-blown transport rates follow either a quadratic or a cubic scaling with the wind shear velocity u_*—which is proportional to the mean flow velocity gradient in turbulent boundary layer flow—depending upon the bed being fully erodible or fully non-erodible, respectively (Creyssels et al., 2009; Ho et al., 2011). Moreover, a quartic scaling of the sand flux with u_*, characterizing a collisional or intense transport regime where the saltation layer is connected to the granular bed through an intermediate granular layer of intense mid-air collisions, has been reported for fully erodible bed conditions when u_* exceeds about $4u_{*t}$, where u_{*t} stands for the minimal threshold

for sustained transport (Pähtz & Durán, 2020; Ralaiarisoa et al., 2020). However, natural Aeolian systems encompass a broad range of soil types characterized by low sand availability on the ground, including bare and crusted soils sparsely covered with mobile sediments (Amir et al., 2014; Shao, 2008). The characteristics of Aeolian transport over such types of soil, that is, when the thickness of the mobile sand layer on the rigid ground is comparable to a few grain diameters, are poorly understood.

The quantitative understanding of these characteristics is important for various fields, in particular to improving wind-blown sand and dust schemes in climate models. Once in the atmospheric circulation, dust substantially affects the planet's climate and biosphere, atmospheric geochemistry, the hydrological cycle, and various other components of the Earth system, yet estimates of vertical dust flux and atmospheric dust budget are counted amongst the largest uncertainty sources in climate simulations (Kok et al., 2012; Mahowald et al., 2014; Schepanski, 2018; Shao, 2008). Since dust is rarely entrained directly by wind but is, instead, emitted mainly by the impacts of wind-blown sand grains onto the ground (Shao et al., 1993), an accurate model for the Aeolian sand transport rates over various types of soil, from fully erodible to fully non-erodible, is required. However, it is difficult to derive such a model from analytical computations alone, given the broad range of natural soil erodibility conditions associated with sparsely covered bare, gravel and crusted soils (Amir et al., 2014; Macpherson et al., 2008; Shao, 2008; Wang et al., 2011).

Therefore, here we perform the direct computation of grain trajectories during Aeolian sand transport by means of particle-based simulations, or Discrete-Element-Method (DEM). This type of simulation has been applied previously to investigate Aeolian transport over fully erodible beds (Carneiro et al., 2011; Comola et al., 2019; Durán et al., 2012), thereby introducing a helpful means to elucidate processes that are difficult to assess in wind tunnel or field experiments, such as the mechanisms of sediment transport very close to the bed. Indeed, using DEM simulations, it is possible to resolve these mechanisms, as well as their impact on the resulting sand flux, without any need for assumptions about the splash process, the rebound dynamics or the modification of the wind profile in the transport layer—which are rather directly computed. As we discuss in the subsequent sections, our DEM simulations show that the scaling of the sand flux with u_* displays considerable and yet unreported dependence on the availability of sand on the ground—characterized here through the thickness of the mobile sediment layer covering the non-erodible surface.
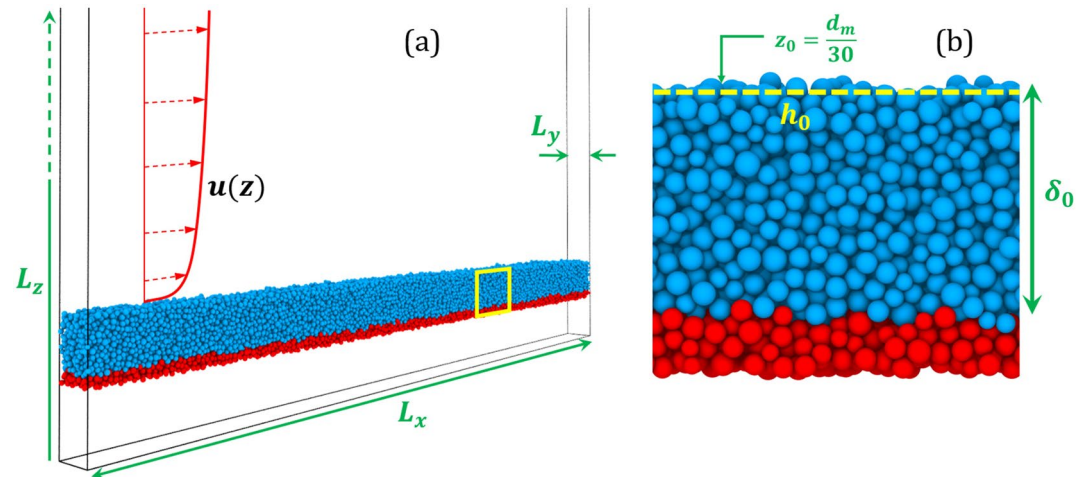
2. Numerical Experiments

The DEM consists of solving Newton's equations of motion for all particles in the system under consideration of the main forces acting on them (Cundall & Strack, 1979). In contrast to other types of numerical models of soil erosion (Almeida et al., 2008; Anderson & Haff, 1988; Kok & Renno, 2009), DEM models of Aeolian transport do not rely, thus, on a splash function to represent the ejection of particles from the soil owing to grain-bed collisions. Rather, the lift-off velocities of the rebound and ejected particles are obtained by directly solving their equations of motion under consideration of particle-particle interactions (Lämmel et al., 2017; Yin et al., 2021).

We start our simulations by pouring sand-sized spherical particles of diameter d uniformly distributed in the range $160 \leq d/\mu m \leq 240$ onto a flat horizontal rigid bed at the bottom of the simulation domain—which has dimensions $(L_x \times L_y \times L_z)/d_m = (200 \times 8 \times 1,000)$, with $d_m = 200$ μm denoting the mean grain size (Figure 1). In doing so, we generate a thin bed of N_p randomly poured particles on the ground, where the bed thickness δ_0 is determined by N_p. For instance, $N_p = 30,000$ for $\delta_0 \approx 15$ d_m.

Furthermore, we adopt periodic boundary conditions in the along-wind (x) and cross-wind (y) directions and impose a reflective horizontal wall at the top of the simulation domain, to avoid that particles escape through crossing the upper boundary at $z = L_z$. However, we find that removing this reflective wall would allow only few particles for escaping, thus leading to a negligible change in the results of our simulations.

Once the particles come to rest and the bed has been formed, a few particles are injected into the simulation domain to impact on the ground, thus producing a splash and ejecting grains into air. The Aeolian drag force on the particles is computed with the expression,

$$\mathbf{F}_i^d = -\frac{\pi d_i^2}{8} \rho_f C_i^d \upsilon_i^r \mathbf{v}_i^r, \tag{1}$$

Figure 1. (a) Snapshot of the numerical experiment at $t = 0$, indicating the dimensions of the simulation domain and the undisturbed wind profile. (b) Side-view of an excerpt of the sediment bed, displaying a layer of mobile particles (blue) of thickness δ_0 on top of the immobile particles constituting the rough ground.

where $\rho_{\mathrm{f}} = 1.225 \ \mathrm{kg/m^3}$ is the air density and $\mathbf{v}_i^{\mathrm{r}} = \mathbf{v}_i - \mathbf{u}(z_i)$ is the difference between the velocity $\mathbf{v}_i$ of particle i and the wind velocity $\mathbf{u}(z_i)$ at the height z_i of the particle's center of mass. Furthermore, $v_i^{\mathrm{r}} = |\mathbf{v}_i^{\mathrm{r}}|$, while the drag coefficient C_i^{d} is computed trough (Cheng, 1997) $C_i^{\mathrm{d}} = \left[(32/\mathrm{Re}_i)^{2/3} + 1\right]^{3/2}$, where the Reynolds number $\mathrm{Re}_i = \rho_{\mathrm{f}} v_i^{\mathrm{r}} d_i / \mu$, with $\mu = 1.8702 \times 10^{-5} \ \mathrm{kg \, m^{-1} \, s^{-1}}$ denoting the dynamic viscosity of the air.

The wind velocity profile is constant along x and y throughout the simulations, while the initial vertical profile of the horizontal (downstream) wind velocity, $u_x(z)$, reads,

$$u_x(z) = \frac{u_*}{\kappa} \ln \frac{z - h_0 + z_0}{z_0} \tag{2}$$

where u_* is the wind shear velocity, $\kappa = 0.4$ the von Kármán constant, $z_0 \approx d_{\mathrm{m}}/30$ is the roughness of the quiescent bed, and h_0 is the bed height, which is set as the uppermost height within the granular surface where the particles move with velocity smaller than $0.1 \, u_*$ (Carneiro et al., 2011). However, the acceleration of the particles owing to the action of the drag force extracts momentum from the air (Anderson & Haff, 1988; Owen, 1964), thus leading to a modification of the wind velocity profile. The modified velocity profile is obtained by numerical integration of (Carneiro et al., 2011)

$$\frac{\partial u_x}{\partial z} = \frac{u_{\tau,x}(z)}{\kappa z}; \ u_{\tau,x}(z) = u_* \left[1 - \frac{\tau_{\mathrm{p}}(z)}{\rho_{\mathrm{f}} u_*^2}\right]^{1/2}, \tag{3}$$

where $\tau_{\mathrm{p}}(z)$ is the grain-borne shear stress and is given by

$$\tau_{\mathrm{p}}(z) \approx \sum_{j \, : \, Z_j > z} \frac{\mathcal{F}_x^{\mathrm{d}}(Z_j)}{A}, \tag{4}$$

with $\mathcal{F}_x^{\mathrm{d}}(Z_j)$ denoting the horizontal component of the total drag force on the particles with center of mass at Z_j, while $A = L_x \cdot L_y$ (Carneiro et al., 2011).

Furthermore, in order to obtain a rough rigid bed underneath the mobile sand cover, we deposit the mobile particles on top of a sheet of "frozen" immobile particles as displayed in Figure 1 (see Supporting Information S1 for the set of DEM particle-particle contact force equations, including the presence of the frozen particles). In doing so, the rigid bed provides a model for a fully consolidated dune surface or bare granular surface, where the constituent immobile particles have the same diameter as the mobile grain size.
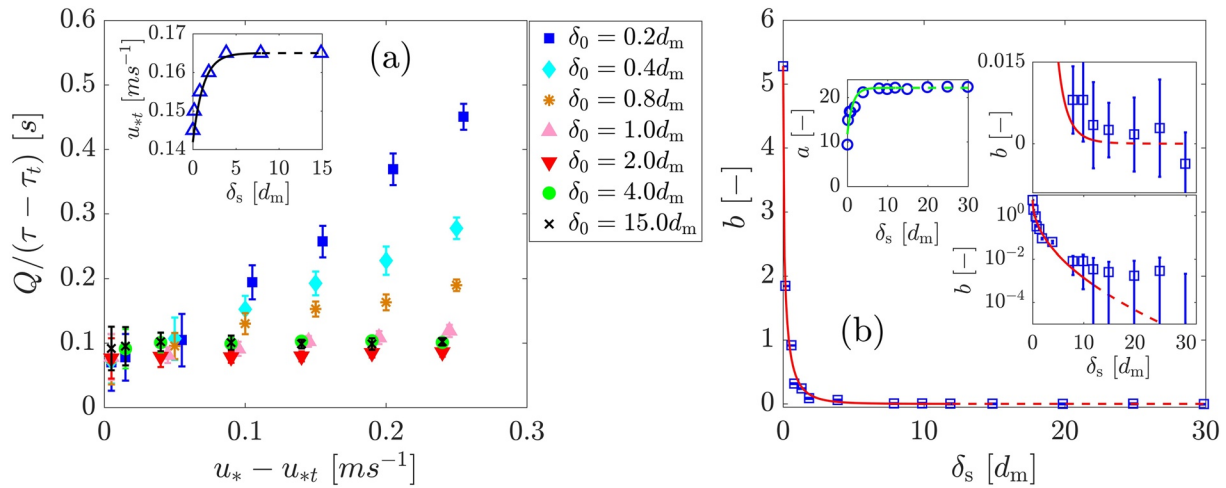
Figure 2. (a) Sand flux Q rescaled with the excess shear stress, $\tau - \tau_t$, plotted as a function of $(u_* - u_{*t})$ for different values of the initial bed thickness, δ_0; inset: the minimal threshold shear velocity for sustained transport, u_{*t} as a function of the steady-state bed thickness, δ_s. (b) Circles and squares denote the parameters a and b in Equation 5, respectively, as obtained from the best fit to the data in (a). The continuous lines in (a) and (b) denote the best fits using Equations 6–8 in the range $\delta_s/d_m \leq 10$ (the continuation of these fits toward larger δ_s/d_m or fully erodible bed scenario is indicated by the dashed line as a guide to the eye). Error bars denote the standard deviation from averaging over 5s within the steady state.

3. Results and Discussion

Once transport begins, some of the grains composing the initial bed layer are entrained into flow, so that the bed layer thickness—which has initial value δ_0 at time $t = 0$—decreases over time until transport eventually achieves steady state. At steady state, the bed layer thickness amounts to $\delta_s/d_m = \left(\delta_0/d_m - C_b u_*/\sqrt{g d_m}\right) \cdot \Theta\left(\delta_0/d_m - C_b u_*/\sqrt{g d_m}\right)$, where $C_b \approx 0.02$ is an empirical parameter and $\Theta(x)$ denotes the Heaviside function, that is, $\Theta(x) = 1$ if $x \geq 0$ and $\Theta(x) = 0$ if $x < 0$ (see Figure S3 in Supporting Information S1). Therefore, the term $C_b u_*/\left(\sqrt{g d_m}\right)$ ($\lesssim 0.5$ for all scenarios) denotes the thickness of the total eroded layer, relative to the particle size, from the beginning of transport until steady state.

We note that periodic boundary conditions are applied in our simulations (see Section 2), so that the number of particles in the system is constant over time (Carneiro et al., 2011; Durán et al., 2012; Pähtz & Durán, 2020). Indeed, the domain of our simulations may be interpreted as a small stretch of soil over which the sediment flux is in the steady state. Due to fluctuations associated with the transport dynamics, the difference between the particle mass outflux from and influx into this soil stretch varies over time, but on average, the total number of particles within the associated volume is constant over time.

We begin our discussion by considering an initial bed thickness $\delta_0 = 15 d_m$, for which we observe steady-state transport conditions ($\delta_s \approx 14.8\ d_m$) consistent with the fully erodible bed scenario reported in previous studies. Specifically, our simulations reproduce quantitatively the height-integrated, non-suspended mass flux of transported particles, Q, as a function of u_* over fully erodible beds, and the observation that, for moderate wind conditions ($u_*/u_{*t} \lesssim 4$), Q is approximately proportional to $\tau - \tau_t$, with $\tau = \rho_f u_*^2$ denoting the mean shear stress of the turbulent wind flow over the surface, and $\tau_t = \rho_f u_{*t}^2$ corresponding to the minimal threshold τ for transport (Figure 2). Furthermore, our numerical predictions match the experimental observations of the nearly exponential decay of the vertical particle concentration with the height above the ground and the value of $u_{*t} \approx 0.165$ m/s predicted for the mean particle size in our simulations (see Figure S1 in Supporting Information S1).

However, as we decrease the initial bed layer thickness δ_0 substantially, we observe a change in the scaling of the steady-state sediment flux with u_*. More precisely, our simulation results follow, approximately, the model.

$$Q = \left\{a \cdot \left[1 + b \cdot \left(\frac{u_*}{u_{*t}} - 1\right)\right]\right\} \cdot \sqrt{\frac{d}{g}} \cdot [\tau - \tau_t], \tag{5}$$

$$u_{*t} = u_{*t,\infty} \cdot \left\{1 - C_t \cdot \exp\left[-c_t \cdot \delta_s/d_m\right]\right\} \tag{6}$$

$$a = a_\infty \cdot \left\{ 1 - C_a \cdot \exp\left[-c_a \cdot \delta_s / d_m \right] \right\} \tag{7}$$

$$b = b_\infty \cdot \exp\left[-c_b \sqrt{\delta_s / d_m} \right] \tag{8}$$

where $u_{*t,\infty} \approx 0.165$ m/s, $a_\infty \approx 22.15$ and $b_\infty \approx 5.28$ denote the values of u_{*t} and the empirical constants a and b, respectively, associated with fully erodible bed scenario ($\delta_s / d_m \to \infty$), while the best fits to the simulation data in the range $\delta_s / d_m \leq 10$ yield $C_t \approx 0.14$, $c_t \approx 0.83$, $C_a \approx 0.47$, $c_a \approx 0.76$ and $c_b \approx 2.61$ (Figure 2).

Wind tunnel experiments (Ho et al., 2011) revealed a cubic scaling of Q with u_* on fully rigid beds. Here, we find that sediment transport rates over a soil that is not fully rigid but contains, instead, a thin layer of mobile sediment, further depends on this layer's thickness according to Equations 5–8. Specifically, the coefficient b in Equation 8 controls the transition from the cubic to the quadratic scaling of Q with u_* in Equation 5 as bed conditions change from fully rigid ($\delta_s = 0$) to fully erodible ($\delta_s \gg d$). Moreover, while the coefficient a provides an attenuating factor for Q near the rigid bed scenario, a decrease in bed thickness reduces the minimal threshold shear velocity, u_{*t}, as we elucidate next.

To shed light on the microscopic origin of Equation 5, we note that momentum conservation yields $Q = [\ell_{hop} / (u_{0\downarrow} - u_{0\uparrow})] \cdot [\tau - \tau_t]$ (Bagnold, 1941; Ho et al., 2011; Sørensen, 2004), where ℓ_{hop} denotes the mean hop length of the saltating particles, while $u_{0\downarrow}$ and $u_{0\uparrow}$ are their mean horizontal impact and lift-off velocities, respectively. Furthermore, ℓ_{hop} and $u_{0\downarrow} - u_{0\uparrow}$ (computed as explained in Section 4 of the Supporting Information S1) are related to the mean horizontal grain velocity $u_0 = (u_{0\downarrow} + u_{0\uparrow})/2$ (or slip velocity) through the approximate scaling expressions $\ell_{hop} \propto u_0^2 / g$ and $u_{0\downarrow} - u_{0\uparrow} \propto u_0$ (Ho et al., 2011), which leads to $Q \approx C_u \cdot (u_0 / g) \cdot [\tau - \tau_t]$, where C_u is an empirical parameter.

An increase in u_* over a fully erodible bed leads to an enhancement of the particle concentration in the transport layer without significantly affecting u_0, so that Q scales quadratically with u_* in the fully erodible bed regime (Ho et al., 2011). By contrast, the transport layer over the hard surface is, for a given saltation flux, much thicker than over an erodible bed because of the non-saturated feedback which keeps a larger wind velocity in the saltation layer (Ho et al., 2011). The weak coupling between the particles and the wind in the transport layer over a fully non-erodible surface results in a linear scaling of u_0 with u_*, thus yielding a cubic scaling of Q with u_* in the fully rigid bed regime (Ho et al., 2011).

Here we find that, in the presence of a thin layer of mobile sand on the hard ground, the scaling of u_0 with u_* further depends on δ_s (Figure 3c). We find that

$$C_u \cdot \frac{u_0}{g} \approx a \cdot \left[1 + b \cdot \left(\frac{u_*}{u_{*t}} - 1 \right) \right] \sqrt{\frac{d}{g}} \tag{9}$$

with $C_u \approx 1.68$, where the RHS of Equation 9 is the multiplicative factor of $[\tau - \tau_t]$ in Equation 5, that is, including the values of u_{*t}, a and b estimated from Figure 2. Therefore, Equation 9 elucidates the microscopic origin of Equation 5. Since all scenarios (δ_0, u_*) considered here are associated with saturated transport conditions in the steady state (see Figure S3 in Supporting Information S1), that is, since the total mass of particles in the transport layer under given $u_* - u_{*t}$ is the same for all values of δ_0 considered, the effect of sand availability on the scaling of $Q(u_*)$ is attributed entirely to the dependence of u_0 on this availability, encoded in the parameters on the RHS of Equation 9. Our simulations further show that, as sand availability decreases and the transport layer expands, transport can be sustained at increasingly lower u_* (Figure 2a and Equation 6). This finding is further consistent with the wind-tunnel observation that u_{*t} over fully rigid beds is lower than over fully erodible beds (Ho et al., 2011).

To the best of our knowledge, our study is the first one to estimate sediment transport rates from direct numerical simulations of particle trajectories under intermediate soil erodibility conditions between fully erodible and fully non-erodible. We find that our results remain approximately valid when the rigid bed underneath the mobile sediment layer is a smooth flat surface. However, the immobile roughness elements on the hard ground have a crucial effect on the value of the Aeolian sand flux.
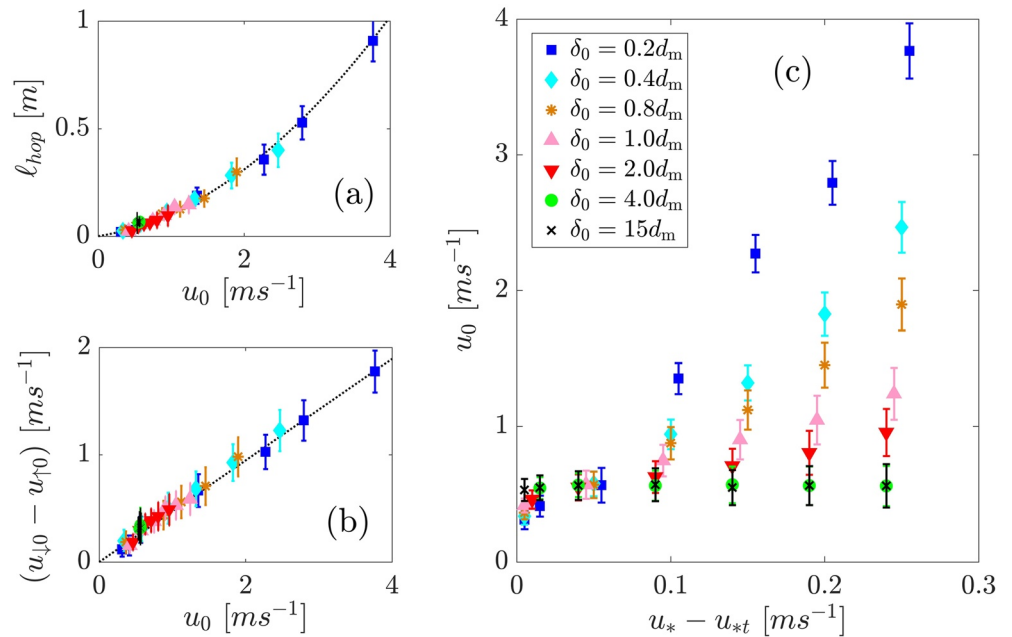
Figure 3. (a) Mean hop length, ℓ_{hop}, and (b) difference between the mean grain horizontal velocities at impact and lift-off, $u_{0\downarrow} - u_{0\uparrow}$, as a function of the slip velocity u_0. The dashed lines in (a) and (b) denote $\ell_{hop} \approx 0.065 u_0^2$ and $u_{0\downarrow} - u_{0\uparrow} \approx 0.43 u_0$, respectively, obtained from the best fits to the simulation data. In (c), the slip velocity is shown as a function of $u_* - u_{*t}$ for different values of δ_0. The legend in (c) applies as well to both (a) and (b).

In the regime where saltating particles collide onto a sand bed of thickness $\lesssim 2 d_m$, and in the presence of roughness elements on the hard ground underneath, sand particles are ejected through splash events mainly *backwards*, that is, the majority of ejecta displays negative horizontal lift-off velocity component. This result can be understood by noting that, as downwind hopping grains impact obliquely upon the thin sand layer covering the rough ground, they mobilize soil grains forward, which, however, collide with the roughness elements located in their front. Upon such collisions, the trajectories of the bed particles mobilized by grain-bed impacts are reflected backwards, as elucidated through our granular splash experiments (Figure 4, where N_{ej} is the number of ejected grains per impact).

These dynamics, which act by attenuating Q upon exposure of the bed roughness elements, are encoded in the coefficient a in Equation 5, and constitute behavior opposite to the effect of the bed thickness on b and u_{*t}, which
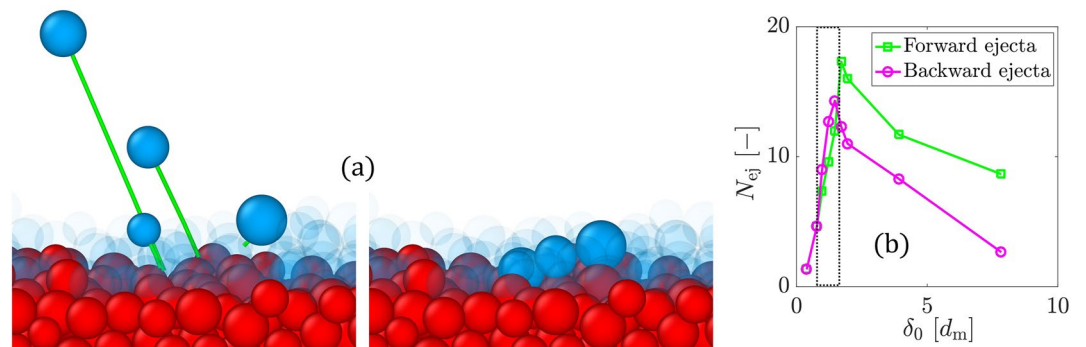
Figure 4. By means of granular splash numerical experiments with impact angles and velocities characteristic of wind-blown sand transport (a), we find that most ejected grains have negative horizontal lift-off velocity, when the value of the bed layer thickness is $\lesssim 2 d_m$, and positive otherwise (b). The snapshots correspond to a simulation using a bed layer thickness $\approx 2 d_m$. Most of the mobile (blue) particles lying on the rigid grains (red) have been rendered transparent for better visualization of the splashed particles.
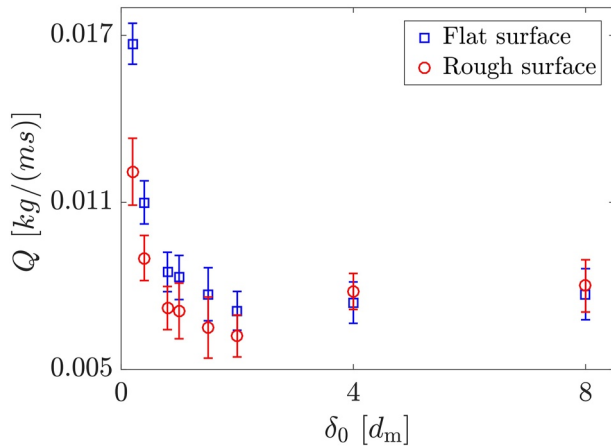
Figure 5. Sand flux Q as a function of δ_0, obtained with $u_* = 0.30$ m/s. We considered the non-erodible surface consisting of a smooth flat ground (blue) and immobile particles (red).

contribute to enhancing Q (see Equations 5–8). These competing effects lead to an anomaly in the dependence of Q on the bed thickness, with the emergence of a minimum around $\delta_0 \approx 2\, d_m$ (or $\delta_s \approx 1.8\, d_m$). This anomaly is not observed when the ground is a smooth flat surface (Figure 5). The bed thickness associated with the minimum Q is independent of u_*, thus indicating that the anomaly reported here is purely a signature of the bed roughness and is not affected by the flow properties.

We note that, notwithstanding the strong decrease of N_{ej} with the bed thickness in the regime $\delta_0/d_m \gtrsim 2$ (Figure 4b), the steady-state sand flux Q in this regime is only weakly affected by the amount of mobile grains on the ground (Figure 2a). Therefore, our simulation results are providing evidence in support of the hypothesis that the magnitude of Q is controlled by the rebound dynamics of sand grains during transport—as assumed, for instance, in a recent purely rebound-based model (Pähtz et al., 2021)—rather than by the splash process. Our results further help to elucidate the observation that cohesion, which affects mainly the splash process by enhancing particle-particle attractive interaction forces within the bed, has little impact on Q and the threshold for Aeolian transport cessation, as these are mainly controlled by rebound dynamics (Comola et al., 2019).

Our model reproduces the scaling laws of Q with u_* observed experimentally over fully erodible and rigid beds (Figures 2 and S1 in Supporting Information S1). However, various ingredients that are essential to improve the quantitative assessment of Aeolian sand flux, such as complex particle geometric shapes and aerodynamic entrainment (Li et al., 2020), should be incorporated in future work. Furthermore, we have employed sand-sized non-erodible roughness elements, but natural soils encompass much broader particle size distributions, including gravels, pebbles and rocks. From our results, we expect that such coarser non-erodible elements have even larger impact on the sand flux scaling. Our model is paving the way toward a quantitative representation of sand availability conditions in larger scale models, such as regional Earth system simulations, by explicitly incorporating the information of local steady-state bed thickness in the parameterization of Aeolian sand transport rates.

Previous work developed continuum models for Aeolian flux that explicitly account for sand supply and spatio-temporal variations in bed surface properties, including moisture, shells, non-erodible elements and vegetation (De Vries et al., 2014; Hoonhout & Vries, 2016). Furthermore, the particle-based simulations adopted in the present work provide a means to improve our understanding of the (microscopic) particle-scale mechanisms controlling the response of Aeolian transport processes to different types of soil and particle-bed interactions. Future research combining insights from both types of model could thus help to achieve improved numerical simulations of Aeolian soil morphodynamic processes at different scales (Durán et al., 2010; Kroy et al., 2002; Werner, 1995), by incorporating the effect of sediment availability on sediment flux and erosion/deposition rates.

4. Conclusions

In conclusion, we have presented the first numerical model for wind-blown sand flux under low sand availability, by characterizing this flux as a function of the thickness of the mobile sediment layer available for transport on the ground. Specifically, we showed that the Aeolian sand flux scales with the excess shear stress multiplied by a coefficient that decreases with the mobile layer thickness covering the non-erodible ground, thereby yielding a model for Aeolian transport rates under intermediate bed erodibility conditions between the fully erodible and fully non-erodible scenarios. Our model elucidates how the scaling of the Aeolian sand flux Q with the wind shear velocity u_* changes from quadratic to cubic as bed conditions change from fully erodible to fully non-erodible, respectively (Ho et al., 2011).

We also found that the roughness elements on the rigid bed affect the sediment flux upon rigid bed exposure, by causing an anomaly in the behavior of Q with the bed layer thickness, with the occurrence of a minimum which is independent on the flow conditions. These findings will have an implication for the representation of non-erodible elements associated with different types of soil in future experimental and theoretical studies.

Data Availability Statement

References

Almeida, M. P., Parteli, E. J. R., Andrade, J. S., & Herrmann, H. J. (2008). Giant saltation on Mars. *Proceedings of the National Academy of Sciences*, *105*(17), 6222–6226. https://doi.org/10.1073/pnas.0800202105

Amir, R., Kinast, S., Tsoar, H., Yizhaq, H., Zaady, E., & Ashkenazy, Y. (2014). The effect of wind and precipitation on vegetation and biogenic crust covers in the Sde-Hallamish sand dunes. *Journal of Geophysical Research: Earth Surface*, *119*(3), 437–450. https://doi.org/10.1002/2013JF002944

Anderson, R. S., & Haff, P. K. (1988). Simulation of eolian saltation. *Science*, *241*(4867), 820–823. https://doi.org/10.1126/science.241.4867.820

Bagnold, R. A. (1941). The physics of blown sand and desert dunes. *The Geographical Journal*, *98*(2), 109. https://doi.org/10.2307/1787211

Carneiro, M. V., Pähtz, T., & Herrmann, H. J. (2011). Jump at the onset of saltation. *Physical Review Letters*, *107*(9), 098001. https://doi.org/10.1103/PhysRevLett.107.098001

Cheng, N.-S. (1997). Simplified settling velocity formula for sediment particle. *Journal of Hydraulic Engineering*, *123*(2), 149–152. https://doi.org/10.1061/(asce)0733-9429(1997)123:2(149)

Comola, F., Gaume, J., Kok, J., & Lehning, M. (2019). Cohesion-induced enhancement of aeolian saltation. *Geophysical Research Letters*, *46*(10), 5566–5574. https://doi.org/10.1029/2019GL082195

Creyssels, M., Dupont, P., El Moctar, A. O., Valance, A., Cantat, I., Jenkins, J. T., et al. (2009). Saltating particles in a turbulent boundary layer: Experiment and theory. *Journal of Fluid Mechanics*, *625*, 47–74. https://doi.org/10.1017/S0022112008005491

Cundall, P. A., & Strack, O. D. (1979). A discrete numerical model for granular assemblies. *Géotechnique*, *29*(1), 47–65. https://doi.org/10.1680/geot.1979.29.1.47

De Vries, S., de Vries, J. V. T., Van Rijn, L., Arens, S., & Ranasinghe, R. (2014). Aeolian sediment transport in supply limited situations. *Aeolian Research*, *12*, 75–85. https://doi.org/10.1016/j.aeolia.2013.11.005

Durán, O., Andreotti, B., & Claudin, P. (2012). Numerical simulation of turbulent sediment transport, from bed load to saltation. *Physics of Fluids*, *24*(10), 103306. https://doi.org/10.1063/1.4757662

Durán, O., Parteli, E. J., & Herrmann, H. J. (2010). A continuous model for sand dunes: Review, new developments and application to barchan dunes and barchan dune fields. *Earth Surface Processes and Landforms*, *35*(13), 1591–1600. https://doi.org/10.1002/esp.2070

Gillette, D. A. (1981). Production of dust that may be carried great distances. In *Desert dust: Origin, characteristics, and effect on man* (pp. 11–26). Geological Society of America. https://doi.org/10.1130/SPE186-p11

Ho, T. D., Valance, A., Dupont, P., & El Moctar, A. O. (2011). Scaling laws in aeolian sand transport. *Physical Review Letters*, *106*(9), 094501. https://doi.org/10.1103/PhysRevLett.106.094501

Hoonhout, B. M., & Vries, S. d. (2016). A process-based model for aeolian sediment transport and spatiotemporal varying sediment availability. *Journal of Geophysical Research: Earth Surface*, *121*(8), 1555–1575. https://doi.org/10.1002/2015JF003692

Kok, J. F., Parteli, E. J., Michaels, T. I., & Karam, D. B. (2012). The physics of wind-blown sand and dust. *Reports on Progress in Physics*, *75*(10), 106901. https://doi.org/10.1088/0034-4885/75/10/106901

Kok, J. F., & Renno, N. O. (2009). A comprehensive numerical model of steady state saltation (COMSALT). *Journal of Geophysical Research*, *114*(D17), D17204. https://doi.org/10.1029/2009JD011702

Kroy, K., Sauermann, G., & Herrmann, H. J. (2002). Minimal model for aeolian sand dunes. *Physical Review E—Statistical Physics, Plasmas, Fluids, and Related Interdisciplinary Topics*, *66*(3), 031302. https://doi.org/10.1103/PhysRevE.66.031302

Lämmel, M., Dzikowski, K., Kroy, K., Oger, L., & Valance, A. (2017). Grain-scale modeling and splash parametrization for aeolian sand transport. *Physical Review E—Statistical Physics, Plasmas, Fluids, and Related Interdisciplinary Topics*, *95*(2), 022902. https://doi.org/10.1103/PhysRevE.95.022902

Lämmel, M., Rings, D., & Kroy, K. (2012). A two-species continuum model for aeolian sand transport. *New Journal of Physics*, *14*(9), 093037. https://doi.org/10.1088/1367-2630/14/9/093037

Li, G., Zhang, J., Herrmann, H. J., Shao, Y., & Huang, N. (2020). Study of aerodynamic grain entrainment in aeolian transport. *Geophysical Research Letters*, *47*(11), e2019GL086574. https://doi.org/10.1029/2019GL086574

Macpherson, T., Nickling, W. G., Gillies, J. A., & Etyemezian, V. (2008). Dust emissions from undisturbed and disturbed supply-limited desert surfaces. *Journal of Geophysical Research*, *113*(F2), F02S04. https://doi.org/10.1029/2007JF000800

Mahowald, N., Albani, S., Kok, J. F., Engelstaeder, S., Scanza, R., Ward, D. S., & Flanner, M. G. (2014). The size distribution of desert dust aerosols and its impact on the Earth system. *Aeolian Research*, *15*, 53–71. https://doi.org/10.1016/j.aeolia.2013.09.002

Owen, P. R. (1964). Saltation of uniform grains in air. *Journal of Fluid Mechanics*, *20*(2), 225–242. https://doi.org/10.1017/S0022112064001173

Pähtz, T., & Durán, O. (2020). Unification of aeolian and fluvial sediment transport rate from granular physics. *Physical Review Letters*, *124*(16), 168001. https://doi.org/10.1103/PhysRevLett.124.168001

Pähtz, T., Liu, Y., Xia, Y., Hu, P., He, Z., & Tholen, K. (2021). Unified model of sediment transport threshold and rate across weak and intense subaqueous bedload, windblown sand, and windblown snow. *Journal of Geophysical Research: Earth Surface*, *126*(4), e2020JF005859. https://doi.org/10.1029/2020JF005859

Pähtz, T., Parteli, E. J. R., Kok, J. F., & Herrmann, H. J. (2014). Analytical model for flux saturation in sediment transport. *Physical Review E*, *89*(5), 052213. https://doi.org/10.1103/PhysRevE.89.052213

Ralaiarisoa, J., Besnard, J.-B., Furieri, B., Dupont, P., El Moctar, A. O., Naaim-Bouvet, F., & Valance, A. (2020). Transition from saltation to collisional regime in windblown sand. *Physical Review Letters*, *124*(19), 198501. https://doi.org/10.1103/PhysRevLett.124.198501

Sauermann, G., Kroy, K., & Herrmann, H. J. (2001). Continuum saltation model for sand dunes. *Physical Review E*, *64*(3), 031305. https://doi.org/10.1103/PhysRevE.64.031305

Schepanski, K. (2018). Transport of mineral dust and its impact on climate. *Geosciences*, *8*(5), 151. https://doi.org/10.3390/geosciences8050151

Shao, Y. (Ed.). (2008). *Physics and modelling of wind erosion*. Springer Netherlands. https://doi.org/10.1007/978-1-4020-8895-7

Shao, Y., & Li, A. (1999). Numerical modelling of saltation in the atmospheric surface layer. *Boundary-Layer Meteorology*, *91*(2), 199–225. https://doi.org/10.1023/A:1001816013475

Shao, Y., Raupach, M., & Findlater, P. (1993). Effect of saltation bombardment on the entrainment of dust by wind. *Journal of Geophysical Research*, *98*(D7), 12719–12726. https://doi.org/10.1029/93JD00396

Sørensen, M. (2004). On the rate of aeolian sand transport. *Geomorphology*, *59*(1–4), 53–62. https://doi.org/10.1016/j.geomorph.2003.09.005

Wang, X., Zhang, C., Wang, H., Qian, G., Luo, W., Lu, J., & Wang, L. (2011). The significance of Gobi desert surfaces for dust emissions in China: An experimental study. *Environmental Earth Sciences*, *64*(4), 1039–1050. https://doi.org/10.1007/s12665-011-0922-2

Werner, B. T. (1995). Eolian dunes: Computer simulations and attractor interpretation. *Geology*, *23*(12), 1107–1110. https://doi.org/10.1130/0091-7613(1995)023<1107:EDCSAA>2.3.CO;2

Yin, X., Huang, N., Jiang, C., Parteli, E. J., & Zhang, J. (2021). Splash function for the collision of sand-sized particles onto an inclined granular bed, based on discrete-element-simulations. *Powder Technology*, *378*, 348–358. https://doi.org/10.1016/j.powtec.2020.10.008

References From the Supporting Information

Brilliantov, N. V., Spahn, F., Hertzsch, J.-M., & Pöschel, T. (1996). Model for collisions in granular gases. *Physical Review*, *53*(5), 5382–5392. https://doi.org/10.1103/PhysRevE.53.5382

Carneiro, M. V., Araújo, N. A. M., Pähtz, T., & Herrmann, H. J. (2013). Midair collisions enhance saltation. *Physical Review Letters*, *111*(5), 058001. https://doi.org/10.1103/PhysRevLett.111.058001

Di Renzo, A., & Di Maio, F. P. (2004). Comparison of contact-force models for the simulation of collisions in dem-based granular flow codes. *Chemical Engineering Science*, *59*(3), 525–541. https://doi.org/10.1016/j.ces.2003.09.037

Fan, F., Parteli, E. J. R., & Pöschel, T. (2017). Origin of granular capillarity revealed by particle-based simulations. *Physical Review Letters*, *118*(21), 218001. https://doi.org/10.1103/PhysRevLett.118.218001

Fryberger, S. G., Al-Sari, A. M., Clisham, T. J., Rizvi, S. A. R., & Al-Hinai, K. G. (1984). Wind sedimentation in the Jafurah Sand Sea, Saudi Arabia. *Sedimentology*, *31*(3), 413–431. https://doi.org/10.1111/j.1365-3091.1984.tb00869.x

Kruggel-Emden, H., Simsek, E., Rickelt, S., Wirtz, S., & Scherer, V. (2007). Review and extension of normal force models for the discrete element method. *Powder Technology*, *171*(3), 157–173. https://doi.org/10.1016/j.powtec.2006.10.004

Luding, S. (2008). Cohesive, frictional powders: Contact models for tension. *Granular Matter*, *10*(4), 235–246. https://doi.org/10.1007/s10035-008-0099-x

Machado, M., Moreira, P., Flores, P., & Lankarani, H. M. (2012). Compliant contact force models in multibody dynamics: Evolution of the hertz contact theory. *Mechanism and Machine Theory*, *53*, 99–121. https://doi.org/10.1016/j.mechmachtheory.2012.02.010

Parteli, E. J. R., Schmidt, J., Blümel, C., Wirth, K.-E., Peukert, W., & Pöschel, T. (2014). Attractive particle interaction forces and packing density of fine glass powders. *Scientific Reports*, *4*(1), 6227. https://doi.org/10.1038/srep06227

Plimpton, S. (1995). Fast parallel algorithms for short-range molecular dynamics. *Journal of Computational Physics*, *117*(1), 1–19. https://doi.org/10.1006/jcph.1995.1039

Pöschel, T., & Schwager, T. (2005). *Computational granular dynamics*. Springer Berlin Heidelberg.

Santos, A. P., Bolintineanu, D. S., Grest, G. S., Lechman, J. B., Plimpton, S. J., Srivastava, I., & Silbert, L. E. (2020). Granular packings with sliding, rolling, and twisting friction. *Physical Review E—Statistical Physics, Plasmas, Fluids, and Related Interdisciplinary Topics*, *102*(3), 032903. https://doi.org/10.1103/PhysRevE.102.032903

Schäfer, J., Dippel, S., & Wolf, D. E. (1996). Force schemes in simulations of granular materials. *Journal of de Physique I France*, *6*(1), 5–20. https://doi.org/10.1051/jp1:1996129

Schmidt, J., Parteli, E. J., Uhlmann, N., Wörlein, N., Wirth, K.-E., Pöschel, T., & Peukert, W. (2020). Packings of micron-sized spherical particles: Insights from bulk density determination, X-ray microtomography and discrete element simulations. *Advanced Powder Technology*, *31*(6), 2293–2304. https://doi.org/10.1016/j.apt.2020.03.018

Shao, Y., & Lu, H. (2000). A simple expression for wind erosion threshold friction velocity. *Journal of Geophysical Research*, *105*(D17), 22437–22443. https://doi.org/10.1029/2000JD900304

Silbert, L. E., Ertaş, D., Grest, G. S., Halsey, T. C., Levine, D., & Plimpton, S. J. (2001). Granular flow down an inclined plane: Bagnold scaling and rheology. *Physical Review E*, *64*(5), 051302. https://doi.org/10.1103/PhysRevE.64.051302

Verbücheln, F., Parteli, E. J. R., & Pöschel, T. (2015). Helical inner-wall texture prevents jamming in granular pipe flows. *Soft Matter*, *11*(21), 4295–4305. https://doi.org/10.1039/c5sm00760g